A scalable electron beam irradiation platform applied for allotropic carbon transformation

João Paulo de Campos da Costa[a, b], Vinícius Teodoro[b], Marcelo Assis[b], Jefferson Bettini[c], Juan Andrés[e], João Paulo Pereira do Carmo[a,d], Elson Longo[b].

a. Department of Electrical Engineering (SEL), University of São Paulo (USP), 13566-590, São Carlos, SP, Brazil.

b. Department of Chemistry, INCTMN-CDMF, Federal University of São Carlos (UFSCar), 13565-905, São Carlos, SP, Brazil.

c. Brazilian Nanotechnology National Laboratory (LNNano), Brazilian Center for Research in Energy and Materials (CNPEM), 13083-970 Campinas, Brazil.

d. R&D Centre MicroElectroMechanics (CMEMS), University of Minho, Campus Azurem, 4800-052, Guimaraes, Portugal.

e. Department of Analytical and Physical Chemistry, University Jaume I (UJI), 12071, Castelló, Spain

Abstract

The design of solid-state materials whose properties and functions can be manipulated in a controlled manner by the application of electron beam irradiation is important in modern materials chemistry and physics. In this paper, we present a progress in the development of scalable electron beam irradiation platform to obtain innovative materials for technological and industrial applications, since one of the problems to be solved in this research area is the scalability of these new nanomaterials induced by electron beam irradiation (EBI). In particular, we focus on carbon structures due to its excellent and exciting properties applied in the technological area in the last years, where we show for the first time a new strategy for carbon allotropic transformation through the portable EBI. This new platform is particularly effective, fast, versatile, clean and easy-to-use, facilitating the preparation of many types of nanomaterials that cannot be obtained by conventional chemical and physical methods. The EBI on flat graphite pellets resulted in a covering of it surface with rod-like particles composed of different allotropic forms of carbon. Furthermore, the developed system allowed the implantation of the Fe as a catalytic material through steel sputtering of the high voltage acceleration anode during the EBI process. It was observed by HRTEM analyses that the rod-like particles are preferentially composed of highly oriented graphite in its bottom, polycrystalline graphite in its middle and magnetite

nanoparticles in its top-

1. Introduction

The development of manufacturing technologies that allow the efficient and sustainable manipulation of the properties and functions of nanomaterials in a straightforward and controlled manner by the application of electrons or light has drawn the attention of several researchers in modern science and engineering[1]. To directly observe the response of materials, the electron beam (EB) source of a transmission electron microscope or scanning electron microscope can be focused on fine sizes (*i.e.* subnanometer sizes) and easily operated to scan a surface up to millimeters.

The evolution of structural and electronic changes under EB irradiation is the focus of many research studies[2,3], which have unveiled related applications[4–8] that open the opportunity to create a versatile tool for nanotechnology[9,10]. The study of EB-matter interactions is a multidisciplinary subject devoted to understand, predict and investigate such phenomena; it provides a new and feasible tool to design the structures of materials at the nanometer or single nanoparticle level, which is essential for both fundamental research[5,11–15] and potential technological applications[16–20].

The progress in this field, from EB-induced material transformations to atomically precise doping and multi-atom assembly, has been undergoing a paradigm shift from atomic realms towards new dynamic concepts able to tailor the magnetic[21,22], electrical[22–24], optical[25], transport and catalytic properties of materials[26–29], which may have applications in nanotechnology[5,30–32]. This phenomenon occurs through a mechanism involving elastic interactions (knock-on mechanism) and excitation-related processes with concomitant appearance of breaking, forming or rearrangement of chemical bonds present in the specimen. Firstly, the electron-hole generation may occur, creating defects, which in turn provoke changes in the microstructure and electronic distribution of the material. Secondly, it may also lead to the formation of phase segregation and lattice defects, such as the production of vacancies[23,33–35] defect clusters and dislocations[36–40], which modify the crystal lattice of the material.

Therefore, there is still plenty of room for significant improvements to gain more insight into the behavior of the materials under EB irradiation. Innovative strategies can be employed to understand the interactions between the electrons and the irradiated solid so as to correctly interpret experiments, minimize artifacts and take advantage of

the EB irradiation. In this way, science and technology are advancing at the same pace, and a new class of phenomena may contribute to novel technological capabilities.

The main novelty of the present work is the development of new equipment for the irradiation of materials by an EB source in order to make the production of materials scalable and viable. The developed EBI equipment brings several inherent advantages over conventional methods (*e.g.* TEM equipment), such as compact size, low cost of manufacturing, wide and uniform EB, possible operation in low and high vacuum, and insertion of gases via a flow control system. In addition, the device offers the user ease and safe operation with a high reproducibility rate. Since this EB processing technology also has high precision, high efficiency, mature control method and fast developing speed, it can be seen as a new and feasible method for the material processing industry. As a result of this investigation, we provide a new strategy for the design of carbon allotropic transformations from graphite to graphene through EB irradiation.

1.1 Electron beam irradiation equipment

The EBI equipment includes a high voltage power source, an electron accelerator and a vacuum chamber. The electron energy is increased by means of three circular non-magnetic stainless-steel anodes (low-, medium- and high-voltage accelerators) designed with a central aperture for the uniform acceleration of electrons. The cathode consists of a piece of non-magnetic stainless-steel material in a tapered shape to focus on the electrons produced from the tungsten (W) filament. Since it is a software-assisted system, it is possible to control some parameters, such as high voltage applied to the three accelerators, electron beam, filament current, heating, cooling units for the specimen holder, gas injection system and vacuum, in order to obtain the reproducibility in materials modification.

A security system against the effects of ionizing radiation (X-rays) from the deceleration of high-energy electrons was implemented. The electron accelerator zones are protected to avoid direct contact with the equipment during the irradiation process. A wireless Geiger counter for mobile devices is used to measure the ionizing radiation (α-, β- and γ-particles, and X-rays). As auxiliary protection, a lead plate housing was designed and implemented against the ionizing radiation generated during the irradiation process. Figure 1 shows a schematic diagram of the EBI equipment.

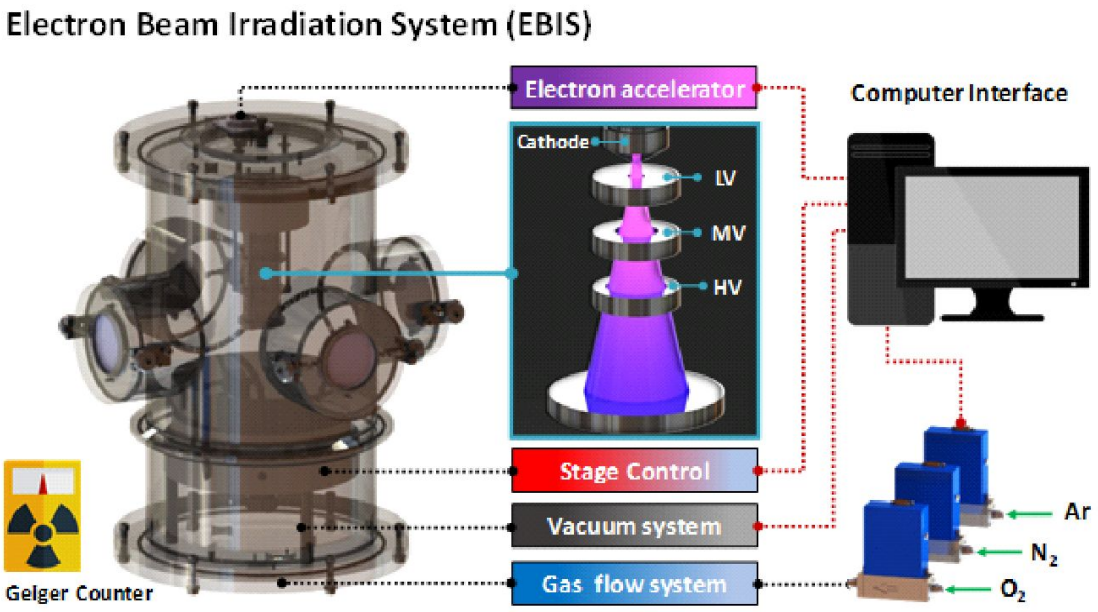

Fig 1 – Schematic representation of the developed electron beam irradiation system (EBIS), showing the main components used for the process automation applied for the allotropic carbon transformation. The EBI system is composed by three voltage acceleration anodes (low voltage - LV, medium voltage – MV, and high voltage - HV), gas injection module, vacuum control and ionizing radiation protection system during the irradiation process.

1.2 Carbon allotropic transformations through electron beam irradiation

As reported in the literature, carbon structures can suffer structural modifications through the interaction with an EB source[41–44] since the morphological modifications are closely related to structural changes[45].

Graphite is formed from stable plates of sp^2 carbon, *i.e.*, three σ bonds and one π bond[46]. These plates have a structure that can receive electrons and undergo profound modifications. When an electron beam strikes the graphite surface, there are inelastic shocks that modify the bonds, bond angles and dihedral angles, forming pseudo sp^3 carbon bonds. As a consequence, there is the formation of a structure similar to a fullerene molecule[43,47,48]. This molecule can turn into a one-dimensional carbon nanotube structure[41,49–52]. This phenomenon occurs because the plates are graphene, which has a single dissolution relationship similar to a photon. In this way, the electron transport is almost perfect, with a quantum transformation reaction to form different carbon structures. In order to acquire a deeper insight into these morphologies, a cross-sectional analysis of all pellets was also performed.

Transition metals such as Fe, Ni, Co, Cr, Os, Ru and Mo can be used to catalyze

the growth of single or multi-walled carbon nanotubes and fullerenes (C_{60}, C_{70}, etc.)[53–57]. The ability of a transition metal to catalyze the formation of carbon nanotubes is directly linked to the possibility of carbon diffusion in these materials, the degradation capacity of carbon compounds and the ability of these metals to form carbides[54,58]. It is also known that the particle size and morphology of the catalyst are directly associated with the nanotube diameter and growth orientation[59–62]. In the electron beam process, the catalytic material from the electron accelerators is transferred to the surface of the graphite pellet. Since the energy of the basal planes of the graphite layers is smaller than that of the catalyst planes, the process of forming cylindrical planes becomes favorable, resulting in the formation of carbon nanotubes[54,63]. The graphite structure is composed of several layers of carbon that interact with each other by van der Waals interactions, forming a packing of layers along the z-axis with a 3D-type structure. Each layer is composed of sp^2-hybridized carbons organized in rings of hexagonal arrangement with a 2D sheet[64–67]. An external disturbance, such as electron beam irradiation, can overcome the Coulombic potential in the van der Waals interaction, resulting in the exfoliation of the graphite structure, and consequently the appearance of a secluded 2D sheet of sp^2 carbons. The exfoliation of graphite leads to the graphene structure, *i.e.*, a few numbers of packaged layers. Since these layers are practically isolated compared to bulk graphite, they exhibit intrinsic behavior and properties due to the lower number of interacting layers that results in higher exposure of delocalized π bonds, which confers the graphene structure unique electrical properties[68].

The carbon allotropy has a diversity of possible structures that can exist from 0 to 3D structures. These structures can become another type by modification processes, such as electron beam irradiation[41,43,48,69], catalytic transformations[42,70–72], etc. As reported by Geim and Novoselov, a graphene sheet is considered as a source for all graphitic forms, behaving as a building material for transformations of all other dimensionalities of carbon structures. A graphene sheet can be wrapped to form fullerene structures (0D), rolled to form carbon nanotubes (1D) and packaged to form graphite structures (3D)[73].

Furthermore, some defects in the graphene sheet can induce changes in the geometry conformation of carbons and the type of carbon rings, leading to structural transformations. One of these transformations is the inverse Stone–Wales (ISW) defect, which causes the migration of carbon atoms to another position in the structure,

resulting in the change from hexagonal to pentagonal and heptagonal rings of carbons. This type of defect is so-called (7557) defect due to the presence of two pentagonal rings sharing two carbon atoms with two adjacent heptagonal rings[74–76]. The most interesting feature of the ISW defects is the transformations that can occur in the 2D carbon sheet, such as the deformation (bending) of the sheet in relation to the z-axis, leading to a convex-like sheet[75]. This deformation originates from the formation of single point defects in the graphene sheet. The deformation of 2D sheet favors the rolling process to form carbon nanotubes. Besides the single defect, multiple ISW defects can also be formed in 2D sheets, that is, the formation of 6 points of ISW defects near each other[74]. These multiple ISW defects are responsible for the formation of 0D fullerene, which are in the form of C_{60} molecule extruded from the 2D graphene sheet by the out-of-plane defects (z-axis). One way to produce ISW defects is by electron beam irradiation of 2D graphene sheets, which in turn tends to induce allotropic transformations of carbon structures[77–79]. In addition, according to the literature the electron beam irradiation of buckminsterfullerene (C_{60}) can induce the coalescence process of this structure, resulting in the formation of carbon nanotubes[41,49,50].

2. Material and methods

2.1 Preparation of pellets for electron beam irradiation

The commercial graphite powder (20 mg for each pellet) was cold-pressed at a pressure of 500 MPa in a die mold with a diameter of 5 mm, resulting in 1mm thickness circular pellets. Three pellets were prepared for each electron beam irradiation time in order to guarantee the reproducibility of the developed system and its use in the characterization techniques.

2.2 EBI process

The graphite pellets were submitted to an irradiation process by the portable developed Electron Beam Irradiation (EBI) system at an acceleration voltage of 20 kV and current of 15 mA for 1, 2, 4, 16 and 8 min. The irradiation was carried out under

low vacuum (10^{-3} mTorr) with a 25mm diameter target area. The different times of electron beam irradiation were proposed in order to observe the electron interaction in the growth of rod-like carbon structures from graphite pellets.

2.3 Characterization

2.3.1 Scanning electron microscopy (FE-SEM) and 3D surface reconstruction

In order to investigate the morphological characteristics of the prepared irradiated pellets as a function of the total electron dose, Field emission gun scanning electron microscopy (FE-SEM) was performed on a FEI microscope (Model Inspect F50) operating at 5 kV.

The images collected by FE-SEM were analyzed and treated with the software Mountains Map Universal, Digital Surf Version 8.0 (Digital Surf, Besançon, France) to generate the 3D reconstruction of the surface topography of all samples. This technique consists of overlapping two captured sample images at different angles to obtain the projection of image depth. The inclination angle of the microscope stage is extremely important to obtain significant 3D information from SEM images that correspond to the identical characteristics of the surface. For this study, for each dose of electron beam irradiation we used the image capture of 0° and 5°. The magnification used was 50,000X, and the work distance was kept constant at 4 mm for both images.

2.3.2 Focused ion beam scanning electron microscopy (FIB-SEM)

A Focused Ion Beam (FIB) FEI Nova 600 Nano Lab microscope with gallium ion sources was used in the characterization and cross-sectional experiments of the graphite structure. The graphite pellet irradiated by electron beam for 32 min was fixed to the sample holder by carbon tape and inserted into the chamber. The stage was then tilted to an angle of 52° and placed at a working distance of 5 mm. A voltage of 16 kV and a current of 0.24 nA were established for the cross-section cut into a circular area with a diameter of 6 mm, in which the cut steps were performed by 100 to 100 nm (FIB video1) in order to observe and understand the growth mechanism of these structures.

The SEM-EDS technique was specifically used in the structure characterization to determine the chemical (qualitative) composition of the material. Energy Scattering

X-Ray Spectrometry analysis (EDS) was performed using an Oxford Instruments X-Max Silicon Drift Detector (SDD) with a 10-kV acceleration voltage to collect the constituent elements of the rod-like structures.

2.3.3 X-Ray diffraction (XRD)

The crystal structure and long-range ordering of all prepared pellets were characterized by X-Ray diffraction (XRD) in a D/Max-2500PC diffractometer (Rigaku, Japan) using Cu Kα radiation (λ = 1.54056 Å) in the range of 10-110° 2θ at a scan rate of 0.5° min^{-1}.

2.3.4 Micro-Raman scattering spectroscopy

Micro-Raman scattering spectroscopy measurements were performed to investigate the structural short-range ordering of the pristine and irradiated graphite pellets using a Bruker spectrometer (model Senterra) with an excitation laser of 785 nm (wavelength) and operating power of 50 mW.

2.3.5 X-ray photoelectron spectroscopy (XPS)

X-ray photoelectron spectroscopy measurements were carried out to determine the surface composition of all pellet samples using a XPS Scienta Omicron ESCA+ spectrometer (Germany) with monochromatic Al K_{α} radiation of 1486.7 eV. The binding energies of all elements were calibrated with reference to the C 1*s* peak at 284.8 eV.

2.3.6 Transmission electron microscopy (TEM)

Transmission electron microscopy analyses were conducted in order to determine and understand the structural properties of the rod-like structures obtained by electron beam irradiation using a JEOL JEM 2100F. EDS measurements with a 200-kV voltage were performed to identify and quantify the elemental composition throughout the rod-like particles.

The graphite pellet irradiated for 32 min was immersed in a beaker containing

isopropyl alcohol and submitted to an ultrasonic bath (frequency) for 2 min, aiming the withdrawal of the rod-like structures formed on the pellet surface. The resulting suspension was dropped in a holy-carbon grid for the TEM analysis.

3. Results and Discussion

3.1 Scanning electron microscopy (FE-SEM) and 3D surface reconstruction

Fig. 2 shows the FE-SEM images of the surface and cross-section of pristine and electron-beam irradiated pellets (2, 4, 8, 16 and 32 min). Fig. 2a-b, Fig. 2c-d, Fig. 2e-f, Fig. 2g-h, Fig. 2i-j, Fig. 2k-l shows the top of view and a cross-section image of G-0, G-2, G-4, G-8, G-16 and G-32 samples, respectively. As it can be seen in Fig. 2a, the surface of the pristine graphite pellet is composed of plates containing a few hundreds of nanometers, resulting in a flat and compact surface. These characteristics were confirmed by the cross-section image in Fig. 2b. As the graphite pellet was exposed to electron beam irradiation for 2 min, a rod-like structure grew throughout its surface (Fig. 2c-d), resulting in a full covering of such surface. With the increase of the irradiation time, these rod-like structures were also observed on the whole surface of the graphite pellets. However, there was an increase in the length of these rods as a function of irradiation time, according to Fig. 2. It can be observed in the cross-section images that these rods grew above the graphite plates. Such structures are expected to arise from the flat surface plates by the transformation of graphite. Besides that, an increase in the rod thickness was also observed with the increase of the irradiation time. This effect became more evident in the pellet irradiated for 32 min (Fig. 2k-l), when a sintering process of adjacent rods occurred.

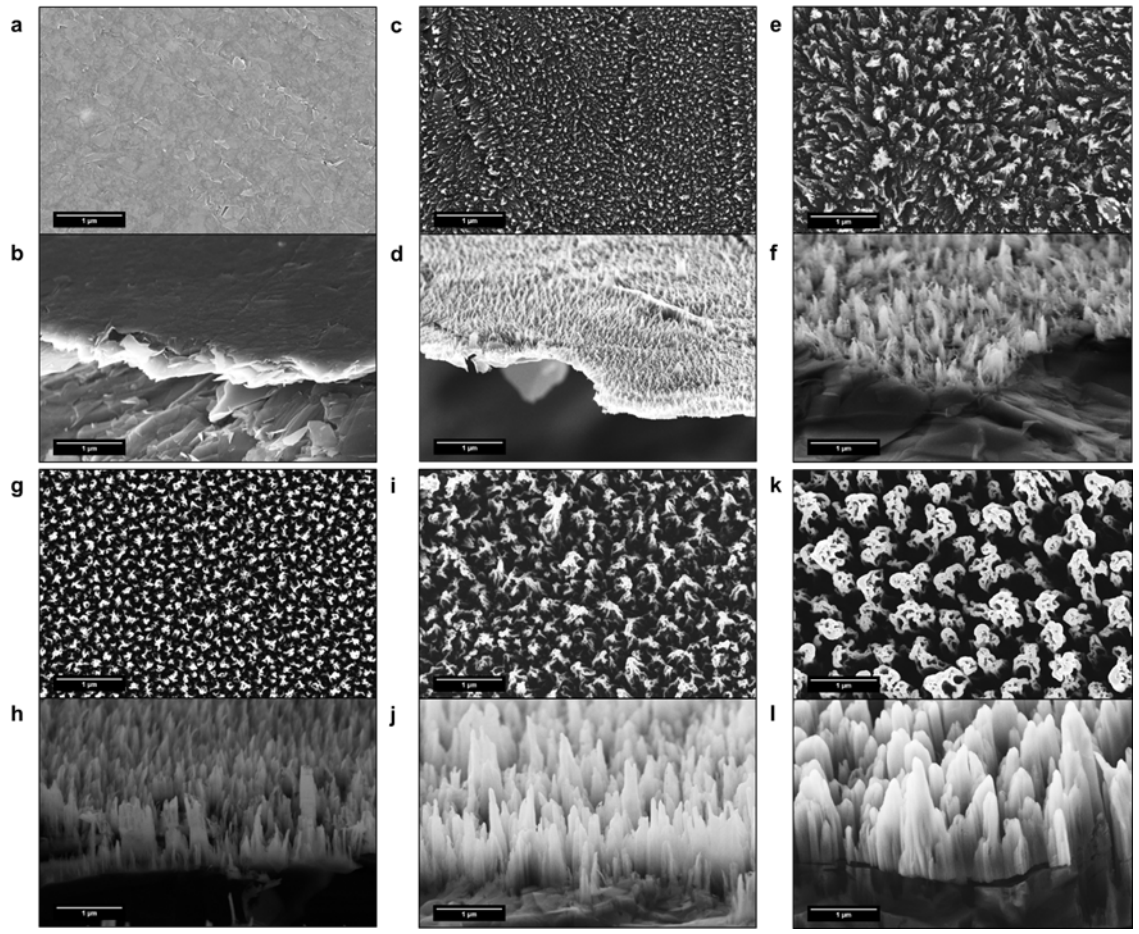

Fig 2 – FE-SEM images of the surface and cross-section of pristine carbon and (a-b) pellets irradiated by electron beam for different times of exposure dose: (c-d) 2 min, (e-f) 4 min, (g-h) 8 min, (i-j) 16 min and (k-l) 32 min, respectively.

Aiming to analyze the rod-like structures generated by electron beam irradiation, the pellet irradiated for 32 min, which presented the longest rods, was immersed in a beaker containing isopropyl alcohol, and subsequently submitted to an ultrasonic bath for 5 min to remove a fraction of the rods from the pellet surface. Fig. 3 displays FE-SEM images of the withdrawn rods, as it is observed in Fig. 3a,b the rods are composed of vertically arranged plates attached to flat horizontal plates in the pellet surface.

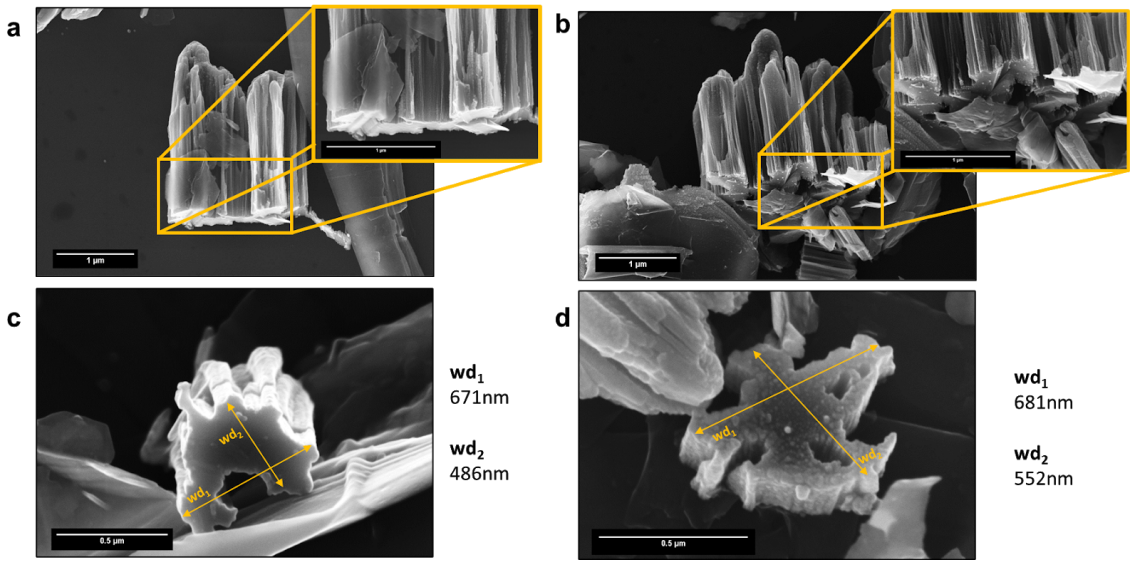

Fig. 4 – FE-SEM images of G-32 (a-b) rod-like particles and respective zoom at the base of the particle structure, (b) bottom view of the rod-like structure and (c) a disrupted region that corresponds to the ground of the rod-like particles and respective average width.

From the disrupted region corresponding to the base of the rod in Fig. 3c,d, we can see a sliding of the graphite layers originating from the graphite plates where the rods started to grow. As a result, there is an increase in the rod width compared to the shorter irradiation times. Another feature regarding the rods is the difference in the morphological structure between the base and the top. It is clearly observed that the top is a region of lower diameter and structure than the base and has a pointed shape. According to this, it is expected that both regions have different physical-chemical behaviors[80]. Although several works studied the effect of electron beam irradiation on graphite samples, the study on morphological rod-like structures such as those obtained in this work is a relatively new subject. It should be noted that three parameters were changed: the high density of electrons in graphite, the low *vacuum* with the existence of a low oxygen density and the presence of iron oxide acting as a catalyst for buckminsterfullerene and carbon nanotubes.

Fig. 4 shows the isometric and cross-sectional view of the 3D surface topography of the pristine and carbon pellets irradiated by electron beam (for 2, 4, 8, 16 and 32 min), where it is possible to see how the formation and growth of these microstructures as well as their topographic characteristics occur according to the irradiation dose (video file1).

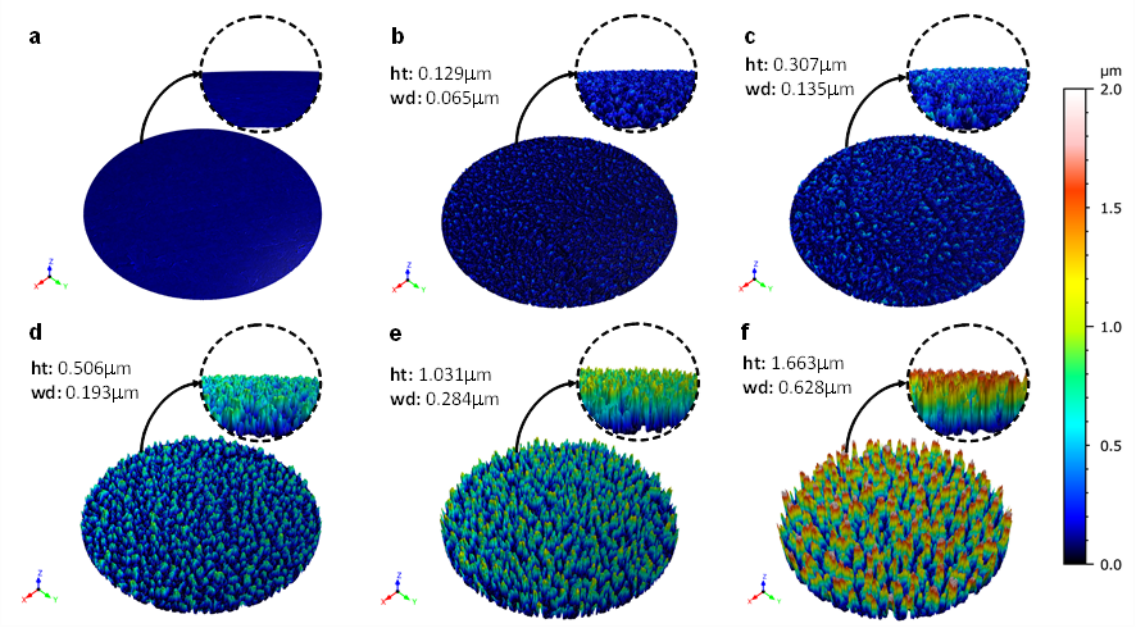

Fig. 4 – 3D reconstruction of the pellet surface with respective height (ht) and width(wd) for each irradiated sample (a) G-0; (b) G-2; (c) G-4; (d) G-8; (e) G-16 and (f) G-32.

In order to verify a trend in the graphite transformation and growth of these rod-like structures, the rod average lengths of these pellets were plotted against the irradiation time (Fig. 6a). We can see that the height and width of the rod-like structure increases with the irradiation time, which was fitted with a polynomial function. Hereupon, the rate constant for the height (k_1) and the width (k_2) for the growth of these rod-like structures as a function of the electron beam irradiation time was obtained by the angular coefficient of the polynomial fit, which was 74.5 nm min^{-1} and 18.9 nm min^{-1} respectively.

3.2 Focused ion beam scanning electron microscopy (FIB-SEM)

Fig. 5 displays scanning electron microscopy (SEM) images of the 32 min pellet area selected for the beam cross-section. Fig. 5a shows the surface of the pellet irradiated for 32 min and Fig. 5b-d display the pruned rods by the gallium ion beam with a prune depth of 0.5, 1.0 and 3.0 µm, respectively.

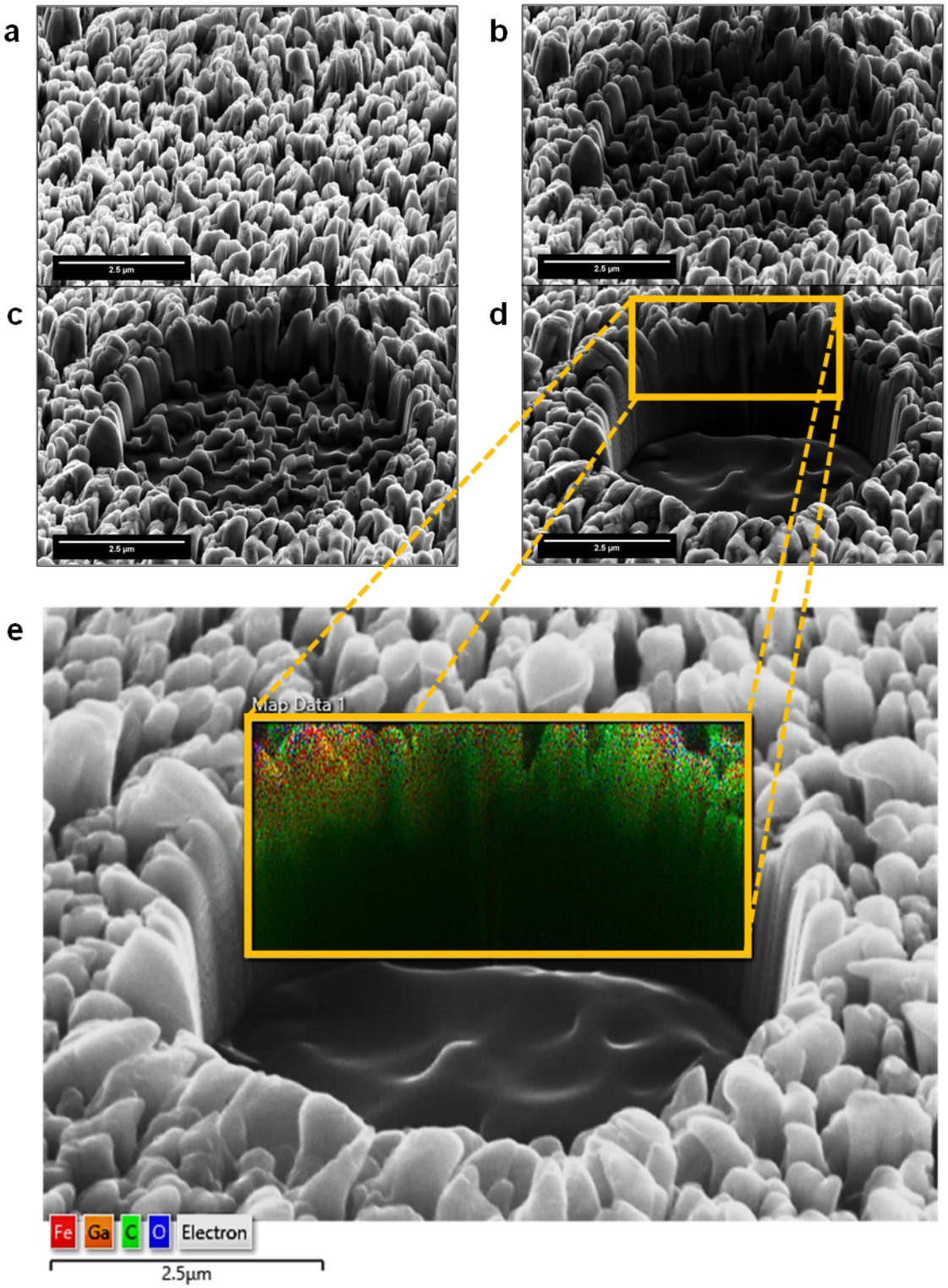

Fig. 5 – (a) FIB-SEM images of the pellet area selected for the beam cross-section; images of the pruned rods by gallium ion beam with prune depth of (b) 0.5, (c) 1.0 and (d) 3.0 µm, respectively, and (e) the area analyzed from the sum of all X-ray collected data during EDS acquisition

Fig. 5e shows the SEM-EDS analysis that was performed in the selected area of the pruned cross-section made by gallium ion beam. The presence of carbon (79.7% σ

0.2), iron (6.1% σ 0.1), oxygen (4.5% σ 0.1) and gallium (9.7% σ 0.1) along the rods was observed after the cross-section made by FIB. However, the EDS analysis indicated a higher proportion of oxygen on the top of the rods compared to the middle and base. As already mentioned, the difference in the morphological structure between the top and base of the rods possibly arises from the difference in structural features. Since the top of the rods has a greater oxygen concentration, the proportion of sp^3 carbon in this region is expected to be higher than that in the middle and base. This sp^3 carbon, especially on the top, appears in form of oxygen-bonded carbon, mainly as hydroxyl, carbonyl, carboxyl, among others[81]. Most of the oxygen on the top of the rods is due to the high exposure surface and consequently the high surface interaction with O_2 in the air compared to the inner structure of the pellet. A transformation in the carbon hybridization occurs when the electron beam irradiates the graphite pellets, turning the sp^2 carbon layered in pristine graphite into oriented graphite and nanographite, followed by an amorphization process to sp^3 carbon. Therefore, on account of the delamination of graphite layers and oxygen-bonded carbon formation, the EDS analysis gave support to the structural transformation and amorphization processes observed by TEM analysis.

3.3 X-ray diffraction (XRD)

Fig. 6b shows XRD patterns of pristine and electron-beam irradiated pellets. As observed, all XRD patterns are in well agreement with hexagonal graphite structure with space group P63/mmc, according to ICSD No. 76767[82]. The well-defined peaks for all samples indicate a high crystallinity degree at long range and an organized packing of sp^2 carbon layers. The peaks located at 26.60°, 42.67°, 44.82°, 54.92°, 60.10°, 77.89°, 83.93°, 85.59° and 87.43° correspond to the reflection of (002), (100), (101), (004), (103), (110), (112), (005) and (006) planes of the graphite structure, respectively. However, when considering the longest rods grown by electron beam irradiation, *i.e.*, the pellet irradiated for 32 min, the thickness of the modified surface is too small compared to that of the whole pellet. Since the intensities of reflections from the graphite planes are relatively high due to the presence of pristine graphite in the bulk pellet, any structural modifications in the rods could not be detected in the XRD patterns because of the very low intensity compared to the bulk graphite. Therefore, the observed peaks of the hexagonal graphite structure in the XRD patterns of all prepared pellets are expected to have emerged from the bulk pristine graphite present in the

pellets.

3.4 Micro-Raman scattering spectroscopy

Fig. 6c exhibits the Raman spectra of all prepared samples performed with an excitation laser of 785 nm (wavelength). The Raman spectra of the graphitic structures showed a characteristic Raman band located at approximately 1580 cm^{-1}, called G band. This band arises from the Raman scattering by doubly-degenerated vibrational modes, namely in-plane optical transverse and in-plane longitudinal phonons in the center of the Brillouin zone[83–85]. Another band characteristic of the graphitic structures is the so-called D band, which arises from transversal optical phonons near the Brillouin zone corner K. This vibrational mode is related to the breathing mode of the six-atom rings of graphite, graphene and graphene oxide structures located at approximately 1350 cm^{-1}[85,86]. For the appearance of this D band, an activation by defects, such as structural disorder, vacancies, strain and edge effect, is required[84,85,87]. The Raman spectra of the pristine and all graphite pellets irradiated by electron beam showed significant intensities of both D and G bands, as seen in Fig. 6c. Another band located at approximately 2700 cm^{-1} related to the double resonance of the D band was observed in all samples[85,88,89].

The Raman band of the sample irradiated for 8 min and higher times showed the emergence of a band located at approximately 690 cm^{-1}, which corresponds to the A_g mode of magnetite (Fe_3O_4), being the characteristic most intense Raman band of this structure[90–92]. This observation corroborated the HRTEM analysis, in which no crystalline structure of magnetite was observed at lower irradiation times, being the Fe disposed of as clusters along with the particle. When the irradiation time is increased to 8 min, these Fe clusters interact with each other to form magnetite nanoclusters, as observed by the presence of Fe_3O_4 particles in the sample irradiated for 32 min. The appearance of the induced disorder of D band for the pristine graphite sample possibly originates from the edge effects associated with the random orientation of graphite sheets throughout the pressed pellets. To evaluate the disorder degree in the graphitic structures by Raman spectroscopy, an analysis of the I_D/I_G ratio is frequently performed, where I_D and I_G are the Raman band intensities of the D and G bands, respectively[93–95].

In order to compare the disorder degree of the pristine and irradiated samples, the I_D/I_G ratio was plotted as a function of electron irradiation time, as shown in Fig. 6d.

As observed, by increasing the irradiation time to 8 min, the I_D/I_G ratio significantly increases and then decreases with higher irradiation times. One of the factors responsible for the appearance and intensity of the D band is the edge effects. Since the electron beam irradiation induces the exfoliation of the graphite sheets to form fullerene and later carbon nanotubes, a great proportion of edges per volume in the initial times of irradiation compared with the pristine graphite would be expected. This is confirmed by HRTEM analysis of the sample irradiated for 2 min, which revealed the presence of giant fullerene particles and polycrystalline graphite. However, by increasing the irradiation time, the multi-walled carbon nanotubes generated from giant fullerene begin to unroll to form a packed structure, the oriented graphite, whose presence was observed during the SAED analysis. The results indicate that this oriented graphite contributes to a decrease in the D-band intensities compared to the G band since the structural disorder is lower than in the polycrystalline structure. In a polycrystalline material, it would be expected a higher density of edges per volume than in a highly oriented and monocrystalline material, thus resulting in a decrease of the I_D/I_G ratio for increasing irradiation time. The presence of a higher proportion of oriented graphite in the sample irradiated by electron beam for 32 min resulted in an I_D/I_G ratio lower than that of the pure graphite.

3.5 X-ray photoelectron spectroscopy (XPS)

Fig. 6e shows the XPS survey spectra of the pristine and pellet samples irradiated by electron beam. As expected, the surface analysis of the pristine graphite indicated only the presence of carbon with a minor proportion of oxygen, while the pellets irradiated by electron beam revealed the presence of these elements together with iron and chromium. Fig. 6f shows the elemental percentage content of surface composition as a function of electron beam irradiation time for all pellet samples. By increasing the irradiation time, the iron content increases until 8 min of irradiation, showing the presence of iron in the surface region, possibly in the edge of giant fullerene structures. Above 8 min of electron beam irradiation, the iron content slightly decreases, possibly indicating the diffusion of magnetite particles to the bulk of the rod-like particles, as observed by the HRTEM analysis. In addition, the oxygen content increases up to 16 min of irradiation, indicating the formation of Fe_3O_4 magnetite structures and amorphous C sp^3 hybrid orbitals. Note that the increase of oxygen content is abrupt until

8 min of irradiation, which is when the emergence of the A_g Raman band of magnetite occurred, confirming the formation of magnetite particles. Along with the decrease in the iron content at higher irradiation times, the oxygen content also decreases on account of the diffusion of magnetite to the bulk of rod-like particles. Nevertheless, a remarkable content of oxygen is still present in the surface region of the sample irradiated for 32 min due to the presence of C sp^3 in its outermost layer, as observed by the HRTEM analysis.

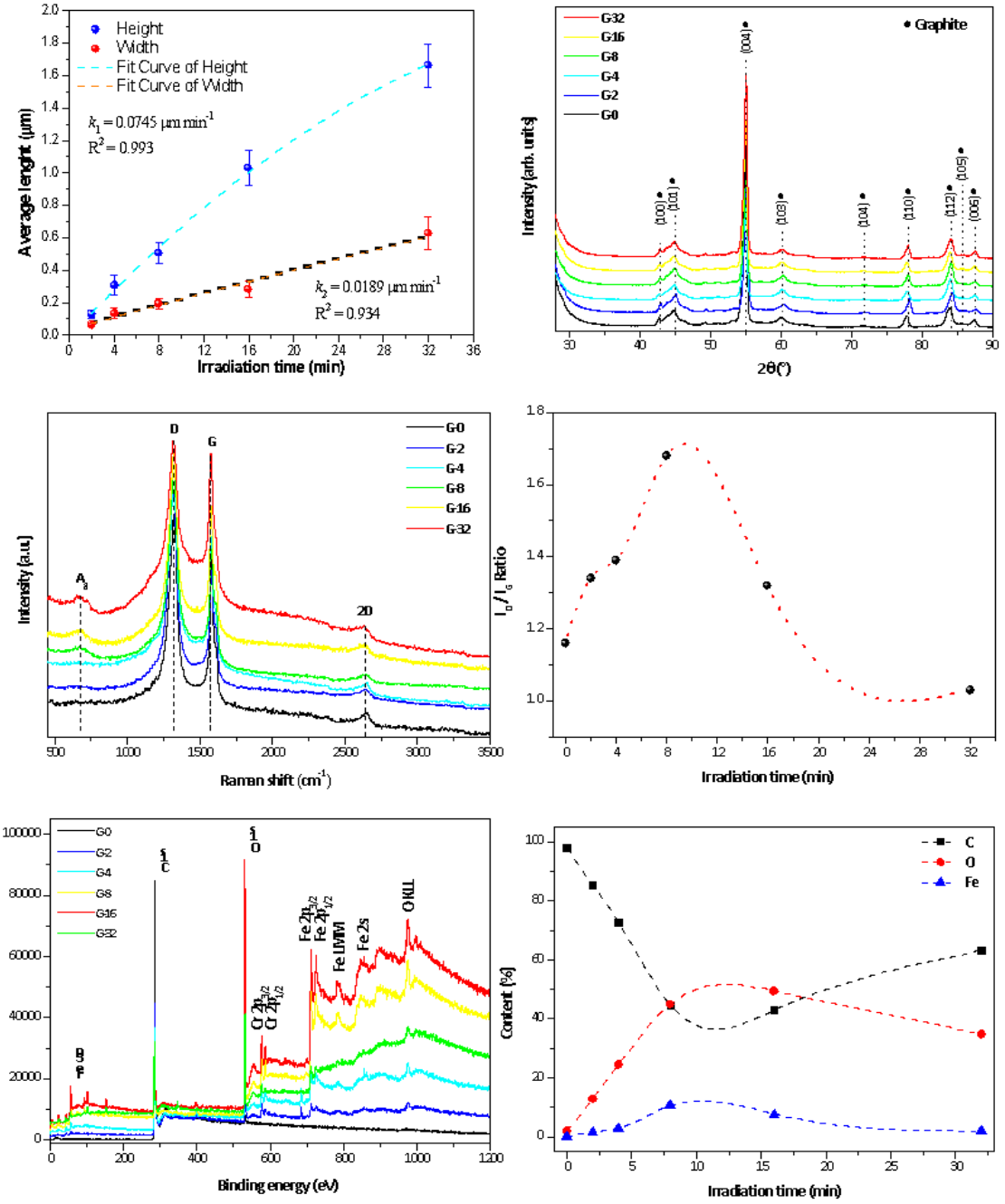

Fig. 6 – (a) Average measurements (n=10) of the lengths and width of the rod like structures for each pellet as a function of irradiation time, (b) XRD patterns of all pellet samples, (c) Micro-Raman spectra of all samples, (d) I_D/I_G ratio against electron beam irradiation time, (e) XPS survey spectra of all samples and (f) Elemental content of surface composition.

3.6 Transmission electron microscopy (TEM)

Fig. 7a shows the TEM image of a rod-like particle withdrawn from the pellet irradiated for 32 min, where an estimated length of 1.64 μm can be seen, which is in good agreement with the average particle length obtained by the FE-SEM analysis. In order to explore such rod-like structure, selected area electron diffraction (SAED) measurements were carried out on the top, middle and base of the withdrawn rods. Fig. 7b-d display TEM images of the rod-like structures with the selected area for the electron diffraction patterns together with their corresponding crystalline planes. The electron diffraction patterns of the base of the rod indicated the presence of well-ordered monocrystalline graphite as the unique structure composing this region as well as a growth oriented to the (002) direction. The (002) plane was identified as the most intense crystalline plane in the graphite structure, with an interplanar distance of 3.39 Å, which is in concordance with the ICSD No. 76767[82]. The SAED analysis of the middle of the rod also showed the presence of monocrystalline graphite with a high degree of orientation towards the (002) direction compared to the base (see Fig. 7d), which can also be related to the reduction in the sample thickness.

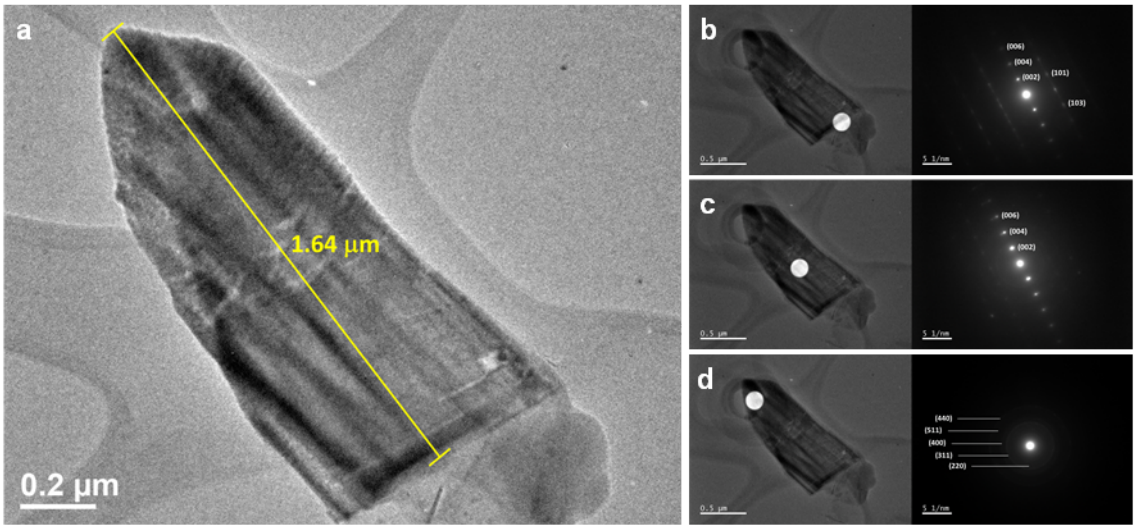

Fig 7 – (a) TEM images of the rod-like particle of G-32 sample with average particle length; TEM image and SAED patterns of the (b) base, (c) middle and (d) top of the

rod-like particle of G-32 sample.

However, the SAED analysis of the top of the rod-like particle showed a different diffraction pattern compared to the other regions (middle and base). As expected in this study, the iron oxide present in the structure was identified as the element composing the particle. According to the SAED results, the diffraction patterns indicated the presence of Fe in the form of Fe_3O_4 (magnetite) cubic structure with Fd-3m space group, which is in well agreement with the ICSD No. 633020[96]. Therefore, it can be concluded that the developed system for electron beam irradiation successfully allowed the implantation of Fe into the sample through steel sputtering of the high voltage acceleration anode during the EBI process, directing the catalysis for oriented growth of monocrystalline graphite.

In order to obtain a better insight into the formation mechanism of the rod-like particle of graphite/magnetite structures, TEM analysis was performed on the graphite pellet irradiated by the electron beam for 2 min. The withdrawal of rod-like particles from the pellet surface followed the same procedure previously described for the pellet irradiated for 32 min. Fig.8a shows the TEM image of a particle irradiated for 2 min and the corresponding fast Fourier transform (FFT) of the selected area in yellow lines. The FFT analysis indicated the presence of polycrystalline graphite and amorphous carbon, according to the (002) plane having an interplanar distance of 3.40 Å. The polycrystallinity of the graphite and a contribution of the amorphous carbon can be clearly observed due to non-periodic fringes random atoms dispersed along the particle. No crystalline particle of magnetite (Fe_3O_4) was observed in the graphite sample irradiated by electron beam for 2 min. However, through EDS analysis of this sample we could note the presence of iron dispersed along the rod-like particle, which were possibly disposed of as clusters, that is, iron-oxygen interactions forming the smaller repeating unit that later generates the crystal structure of magnetite. Because of the relatively short time of electron beam irradiation, these clusters did not have enough energy and time to organize themselves to form periodic repeating units, *i.e.*, the crystalline structure of magnetite.

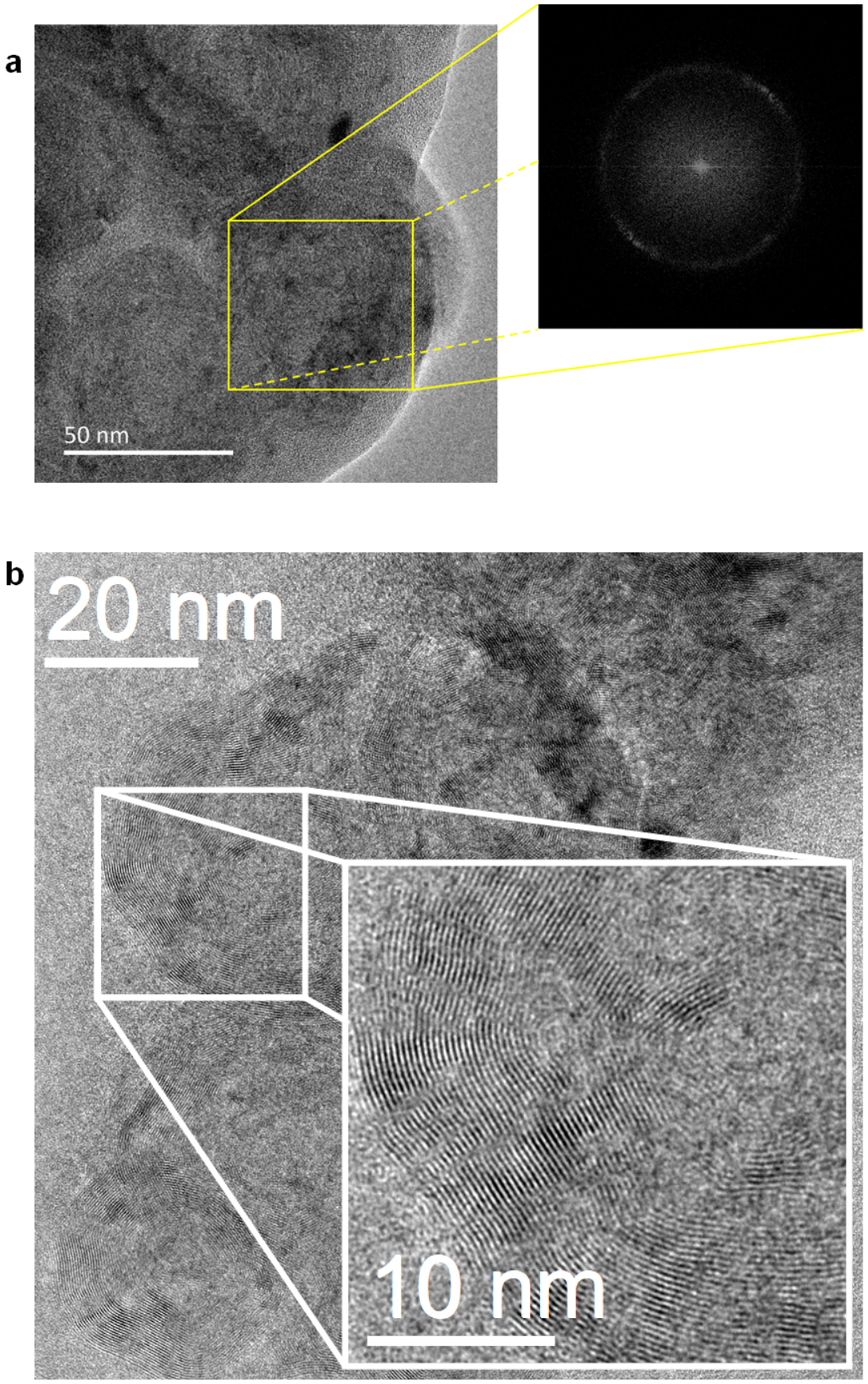

Fig 8 – (a) TEM images of G-2 sample (a) with corresponding FFT of the region marked with yellow lines and (b) respective inset showing the giant fullerene particles.

An interesting morphological structure observed in the graphite pellet sample irradiated for 2 min is the agglomerated spheres, as shown in Fig. 8b. It is well known that fullerene molecules can form multi-shell structures by their self-encapsulation, which results in a larger cage of fullerenes[48,69,97–100]. The resulting structures by this self-increase in fullerene size can also be called either giant fullerene or onion-like fullerene. To form the fullerene cage, a family of this structure is possible presents that comprise a wide range of the number of carbons in fullerene structure[98,101–103]. Among these, C_{60} is the most common and stable fullerene due to its symmetric strain distribution achieved by its spherical form, besides being the smallest fullerene whose pentagons has no other adjacent pentagons sharing carbon atoms[69,101–103]. Mordkovich *et al*.[97] studied the formation of multi-shell fullerene particles by pulsed laser vaporization of a carbon target containing C_{60} species, which results in their encapsulation. Ugarte[69] reported that the electron beam irradiation of carbon soot and tubular graphitic particles by a high-resolution electron microscope induces the formation of onion-like particles. As previously described, the formation of pentagons in the graphite layer induced by electron beam irradiation can also be understood as Stone-Wales inverse defects, resulting in a fullerene. The van der Waals interactions are responsible for the packing of the multiple shells in the fullerene cage[47,104,105].

As reported by Iijima[106], the shape of a multi-shell fullerene is not always perfectly spherical; it appears as an irregular particle in the shells and edges due to the existence of another size of carbon clusters belonging to the family of fullerenes. As proposed by Kroto, the increase in the fullerene size leads to a cage with truncated edges, mainly in the C_{240} and C_{540} fullerenes[107]. According to Ugarte[69], the onion-like particles obtained in his work are composed of C_{60} molecules in the inner and center of the particle with a subsequent curling up of the graphitic shells above this molecule to form a multi-shell particle. The particles reported by Ugarte have an approximate diameter of 47 nm, although some spherical particles with several micrometers of diameter were also found.

The observed agglomerated spheres in the sample irradiated for 2 min provides evidence of fullerene cage formation (giant fullerene). In the magnified region of Fig. 8b, we can note that the particles have a quasi-spherical shape with some truncated edges, indicating the presence of a giant cage of fullerene. The quasi-spherical particles obtained in this work have different diameters of a few nanometers–the particle marked

with a yellow dotted line rectangle has approximately 29.5 nm. Note that the innermost sphere comprised of concentric spherical shells clearly indicates a giant fullerene structure. As previously mentioned, electron beam irradiation is able to induce the coalescence process of fullerene, resulting in extended structures and carbon nanotubes[41,49,50]. This phenomenon can be observed in the orange rectangle in Fig. 8b and the corresponding inset image, in which two giant fullerenes begin to coalesce to form an elongated carbon structure. Since the irradiation time was only 2 min (relatively low electron dose), the coalescence process of fullerene structures was incomplete[41], being possible to observe only the initial step of the elongated carbon structures.

Some transition metals such as Ni[70], Al[72] and Fe[71,108–110] were reported to act as catalysts for the growth of fullerene. The main point here is based on the Fe nanoparticle can improve cutting of graphite layer as Ni NPs cut graphene[111]. In this way, initials buckyballs[112] can be formed and size can increase by temperature[101]. Fig. 8b also shows that some darkest regions are present in the giant fullerene, mainly on the edge of the particles, as observed in the yellow dotted line rectangle. These darkest particles are possibly metallic Fe, which is the main responsible for the catalytic growth of fullerene structures. Fig. 9a displays a surface region of the top of the rod-like particle irradiated by electron beam for 32 min and its corresponding FFT of the selected area. According to the FFT analysis, this region is mainly composed of polycrystalline magnetite (Fe_3O_4) particles, corroborating the SAED results, and by an outermost layer of amorphous carbon.

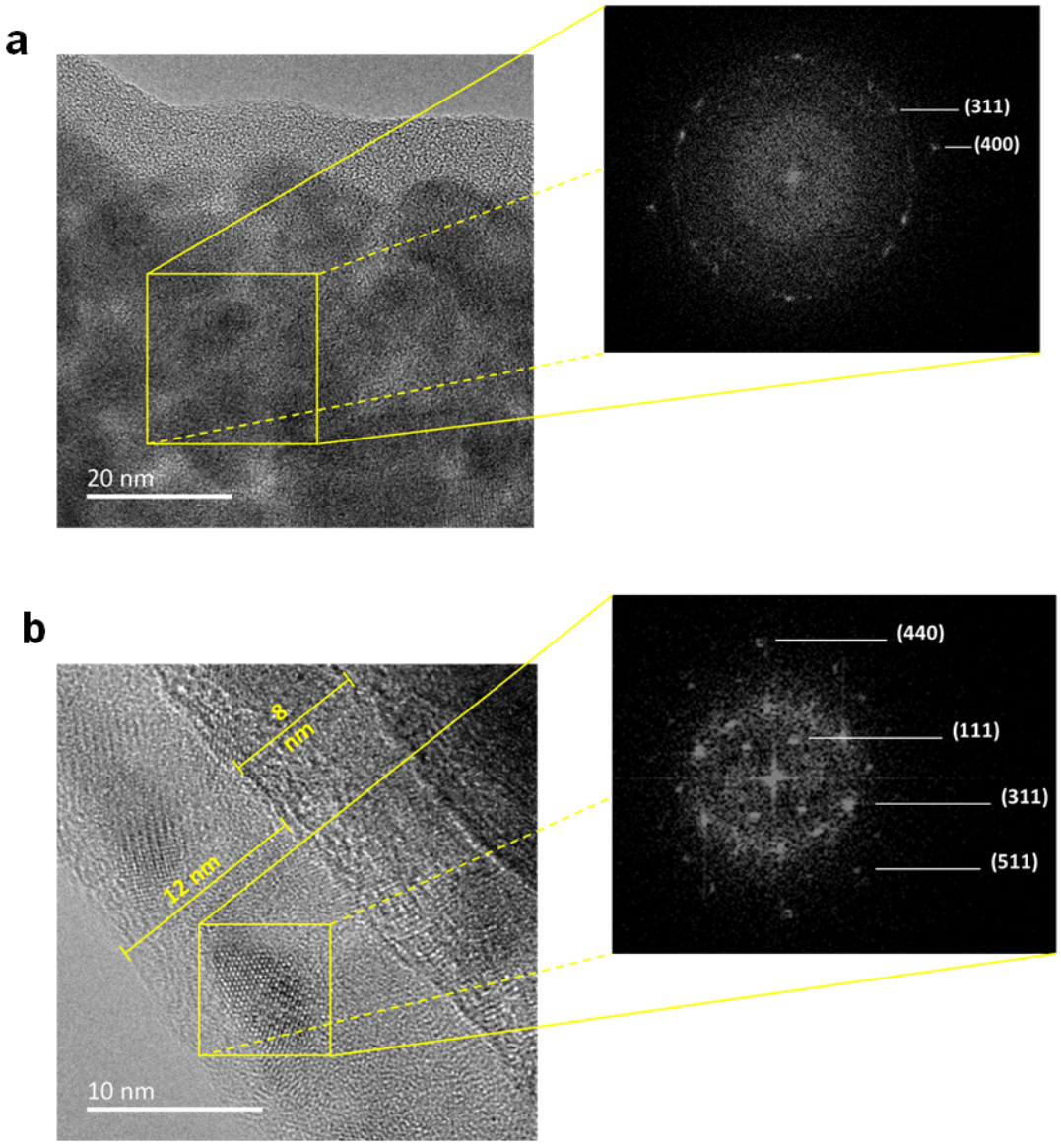

Fig. 9 –HRTEM images of the (a) surface region of the top of the rod-like particle irradiated by electron beam for 32 min and its corresponding FFT, and (b) the dark region corresponding to the dispersed polycrystalline magnetite.

Still in the surface region of the top of this rod-like particle, a dark region corresponding to the dispersed polycrystalline magnetite region can also be observed in Fig. 9b, with a layer of approximately 8 nm in thickness and another (outermost layer) of approximately 12 nm. According to the FFT analysis, this outermost layer is composed of amorphous carbon with embedded magnetite particles. The 8-nm thick layer is seen as a characteristic multi-walled carbon nanotube, with a diameter similar to that obtained by Wirth *et al*., which was approximately 10 nm[109]. Besides the Fe contribution as a catalytic element for fullerene growth, iron oxide was also reported as a catalytic material for the growth of carbon nanotubes[109,110,113]. Morel *et al*.

studied the effectiveness of magnetite particles (Fe_3O_4) as precursors for the synthesis of multi-walled carbon nanotubes (with approximate diameter of 9 nm) by aerosol-assisted chemical vapor deposition[113].

Fig. 10 shows the EDS mapping of a particle from the graphite pellet irradiated by electron beam for 32 min. A higher proportion of carbon (blue distribution) can be seen in the base of the rod-like structure, with a concentration (73.81% σ 0.04) gradient decreasing toward the top of particle. The iron distribution has an opposite behavior compared to carbon, as marked by red distribution, which indicates a higher proportion (14.01% σ 0.03) in the top of the rod-like particle, with a concentration gradient decreasing toward the base. As expected, the presence of oxygen (12.18% σ 0.04) can be observed in the whole particle due to its contribution to the formation of magnetite particles and the amorphous carbon layer on its outermost surface. Fig. 10 also shows the high-angle annular dark-field imaging of the particle and the overlapping of the three colors. Therefore, the EDS analysis corroborated the structural distribution observed by SAED analysis of the whole rod-like particle.

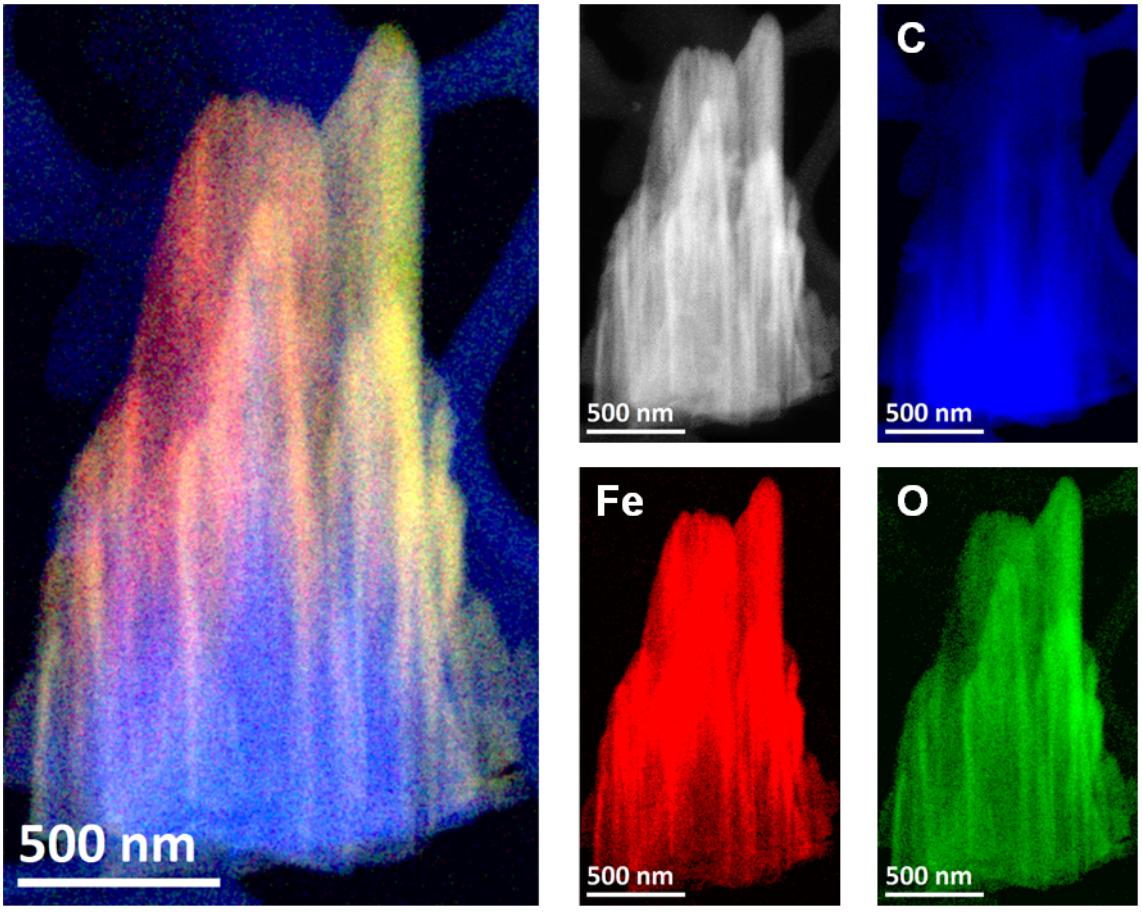

Fig. 10 – HAADF and EDS mapping images of the rod-like particle of G-32 sample showing the elements from the sum of all X-ray collected data during.

It can be concluded that the contribution of Fe in this work is its use as a catalyst for the growth of fullerene particles. After the formation of giant fullerene structures, the electron beam irradiation induces the coalescence of these spherical multi-shell particles, forming the multi-walled carbon nanotubes. It can be noticed that both Fe and Fe_3O_4 particles were observed remaining near the fullerene and multi-walled carbon nanotubes, indicating its release from the carbon structures. As aforementioned, a carbon nanotube can unroll to generate a graphene sheet, which in turn can pack to form the 3D graphite. A possible mechanism for the formation of rod-like particles is the appearance of several multi-walled carbon nanotubes that later undergo an unrolling process of their multi-walls into each separate wall to evolve into the main structure, thus increasing the diameter of the primary particle. In order to better understand the formation mechanism of the vertically distributed rod-like particles by iron implantation and electron beam irradiation, a further study will be conducted to explore more the theoretical and experimental insights.

4. Conclusions

The developed system for electron beam irradiation allowed to obtain and study the morphological and allotropic transformations of graphite structure, as well the implementation of the Fe as a catalytic material for the nucleation of fullerene.

It can be concluded that the developed system for electron beam irradiation successfully allowed the implantation of Fe into the sample through steel sputtering of the high voltage acceleration anode during the EBI process, directing the catalysis for oriented growth of monocrystalline graphite and also the formation of magnetite particles embedded in the carbon structures. The electron beam irradiation induced the curling up process of graphite layers upon the fullerene to form the rod-like carbon structures, with sequential induced coalescence. Moreover, magnetite nanoparticles were observed embedded in the multiwalled carbon nanotubes and in the top of rod-like particles.

We believe that the developed EBI equipment is capable of manipulating nanoparticles and probing the interaction forces between them. For such reason, what we demonstrated here can have a profound impact on physical and chemical sciences and open a new chapter in nanoscience. The present experiment now allows a detailed

atomic resolution study on graphite and its allotropic transformations in carbon nanotubes.

Further work includes a wide range of experiments in nanoscale systems to exploit the atomic precision of the developed EBI equipment as well as to study and understand the correlations between structure–function–technological applications and atomic structure. Therefore, these methods offer the ability to tailor the properties of nano- and micro-materials selectively, being a versatile route to fulfill the one-pot and "green-chemistry" objectives of synthesizing many types of nanomaterials with novel properties and functions. The use of these green synthesis methods could help minimize the toxicity of nanomaterials since they eliminate the use of hazardous and toxic reagents.

Acknowledgements

The authors acknowledge the financial support from Universitat Jaume I for projects UJI-B2016-25 and UJI-B2019-30, and Ministerio de Ciencia, Innovación y Universidades (Spain) project PGC2018-094417-B-I00; Fundação de Amparo à Pesquisa do Estado de São Paulo - FAPESP (2019/18656-6, 2013/07296-2), Conselho Nacional de Desenvolvimento Científico e Tecnológico – CNPq(142035/2017-3), and CAPES. The authors also thank Cesar Fermino Polachini and the Microtube company for manufacturing the mechanical parts of the EBI equipment.

References

[1] R. Ramachandramoorthy, R. Bernal, H.D. Espinosa, Pushing the Envelope of *In Situ* Transmission Electron Microscopy, ACS Nano. 9 (2015) 4675–4685. doi:10.1021/acsnano.5b01391.

[2] R.F. Egerton, Mechanisms of radiation damage in beam-sensitive specimens, for TEM accelerating voltages between 10 and 300 kV, Microsc. Res. Tech. 75 (2012) 1550–1556. doi:10.1002/jemt.22099.

[3] R.F. Egerton, Choice of operating voltage for a transmission electron microscope, Ultramicroscopy. 145 (2014) 85–93. doi:10.1016/j.ultramic.2013.10.019.

[4] J. Andrés, M.M. Ferrer, L. Gracia, A. Beltran, V.M. Longo, G.H. Cruvinel, R.L. Tranquilin, E. Longo, A Combined experimental and theoretical study on the formation of Ag filaments on β-Ag_2MoO_4 induced by electron irradiation, Part. Part. Syst. Charact. 32 (2015) 646–651. doi:10.1002/ppsc.201400162.

[5] I.G. Gonzalez-Martinez, A. Bachmatiuk, V. Bezugly, J. Kunstmann, T. Gemming, Z. Liu, G. Cuniberti, M.H. Rümmeli, Electron-beam induced

synthesis of nanostructures: a review, Nanoscale. 8 (2016) 11340–11362. doi:10.1039/c6nr01941b.

[6] H. Wei, H. Chiu, Y. Ji, B. Wei, X. Lu, X. Han, M.L. Trudeau, K. Zaghib, G.P. Demopoulos, R. Gauvin, *In Situ* TEM Investigation of Electron Irradiation Induced Metastable States in Lithium-Ion Battery Cathodes: Li_2FeSiO_4 versus $LiFePO_4$, ACS Appl. Energy Mater. 1 (2018) 3180–3189. doi:10.1021/acsaem.8b00391.

[7] Q. Zhang, H. Li, L. Gan, Y. Ma, T. Zhai, *In situ* fabrication and investigation of nanostructures and nanodevices with a microscope, Chem. Soc. Rev. 45 (2016) 2694–2713. doi:10.1039/c6cs00161k.

[8] X. Li, J. Qi, Q. Zhang, Z. Wang, Y. Zhang, Investigation of electron beam detection properties of ZnO nanowire based back-to-back double Schottky diode, RSC Adv. 4 (2014) 12743–12747. doi:10.1039/c3ra47934j.

[9] S. V. Kalinin, A. Borisevich, S. Jesse, Fire up the atom forge, Nature. 539 (2016) 485–487.

[10] J. Ran, O.O. Dyck, X. Wang, B. Yang, D.B. Geohegan, K. Xiao, Electron-Beam-Related Studies of Halide Perovskites: Challenges and Opportunities, Adv. Energy Mater. 1903191 (2020) 1–19. doi:10.1002/aenm.201903191.

[11] N. Jiang, Electron beam damage in oxides: a review, Reports Prog. Phys. 79 (2016) 016501. doi:10.1088/0034-4885/79/1/016501.

[12] C. Luo, C. Wang, X. Wu, J. Zhang, J. Chu, *In Situ* Transmission Electron Microscopy Characterization and Manipulation of Two-Dimensional Layered Materials beyond Graphene, Small. 13 (2017) 1604259. doi:10.1002/smll.201604259.

[13] T. Susi, D. Kepaptsoglou, Y. Lin, Q.M. Ramasse, J.C. Meyer, K. Suenaga, J. Kotakoski, Towards atomically precise manipulation of 2D nanostructures in the electron microscope, 2D Mater. 4 (2017) 042004.

[14] X. Zhao, J. Kotakoski, J.C. Meyer, E. Sutter, P. Sutter, A. V Krasheninnikov, U. Kaiser, W. Zhou, Engineering and modifying two- dimensional materials by electron beams, MRS Bull. 42 (2017) 667–676. doi:10.1557/mrs.2017.184.

[15] R.F. Egerton, Beam-induced motion of adatoms in the transmission electron microscope, Microsc. Microanal. 19 (2013) 479–486. doi:10.1017/S1431927612014274.

[16] J.W. Liu, J. Xu, Y. Ni, F.J. Fan, C.L. Zhang, S.H. Yu, A family of carbon-based nanocomposite tubular structures created by *in situ* electron beam irradiation, ACS Nano. 6 (2012) 4500–4507. doi:10.1021/nn301310m.

[17] A. V. Krasheninnikov, F. Banhart, Engineering of nanostructured carbon materials with electron or ion beams, Nat. Mater. 6 (2007) 723–733.

[18] J. Li, Fabrication of a carbon nanotube drive shaft component, Nanotechnology. 15 (2004) 551–554. doi:10.1088/0957-4484/15/5/025.

[19] D. Dupeyrón, J. Rieumont, G. Solorzano, R. Martinez, Formation of carbon-based nanotubular structures by in situ electron irradiation, Nucl. Instruments Methods Phys. Res. Sect. B Beam Interact. with Mater. Atoms. 451

(2019) 18–23. doi:10.1016/j.nimb.2019.04.085.

[20] B. Li, Y. Feng, K.W. Ding, G. Qian, X. Bin Zhang, Y.F. Liu, Effect of electron beam irradiation on multi-walled carbon nanotubes, Trans. Nonferrous Met. Soc. China (English Ed. 24 (2014) 764–769. doi:10.1016/S1003-6326(14)63123-X.

[21] C.J. Benedict, A. Rao, G. Sanjeev, G.S. Okram, P.D. Babu, A systematic study on the effect of electron beam irradiation on structural, electrical, thermo-electric power and magnetic property of $LaCoO_3$, J. Magn. Magn. Mater. 397 (2016) 145–151. doi:10.1016/j.jmmm.2015.08.111.

[22] B. Christopher, A. Rao, U. Deka, S. Prasad K, G.S. Okram, G. Sanjeev, V. Chandra Petwal, V.P. Verma, J. Dwivedi, Electrical, thermal and magnetic studies on 7.5 MeV electron beam irradiated $PrCoO_3$ polycrystalline samples, Phys. B Condens. Matter. 540 (2018) 26–32. doi:10.1016/j.physb.2018.04.026.

[23] B. Christopher, R. Thomas, A. Rao, G.S. Okram, V.C. Petwal, V.P. Verma, J. Dwivedi, A systematic study on effect of electron beam irradiation on electrical properties and thermopower of $RE_{0.8}Sr_{0.2}CoO_3$ (RE=La, Pr) cobaltites, Phys. B Condens. Matter. 552 (2019) 170–177. doi:10.1016/j.physb.2018.10.012.

[24] B.S. Nagaraja, A. Rao, P.D. Babu, G. Sanjeev, G.S. Okram, Influence of electron beam irradiation on the structural, electrical and thermal properties of $Gd_{0.5}Sr_{0.5}MnO_3$ and $Dy_{0.5}Sr_{0.5}MnO_3$ manganites, Nucl. Instruments Methods Phys. Res. Sect. B Beam Interact. with Mater. Atoms. 366 (2016) 188–197. doi:10.1016/j.nimb.2015.11.009.

[25] M. Pattabi, B. Saraswathi Amma, K. Manzoor, Ganesh Sanjeev, Effect of 8 MeV electron irradiation on the optical properties of PVP capped CdS nanoparticles in PVA matrix, Sol. Energy Mater. Sol. Cells. 91 (2007) 1403–1407. doi:10.1016/j.solmat.2007.04.015.

[26] K. Song, D.J. Sauter, J. Wu, V.P. Dravid, P.C. Stair, Evolution of high-energy electron beam irradiation effects on zeolite supported catalyst: Metal nanoprecipitation, ACS Catal. 2 (2012) 384–390. doi:10.1021/cs300002c.

[27] S. Krishnan, G. Sanjeev, M. Pattabi, X. Mathew, Effect of electron irradiation on the properties of CdTe/CdS solar cells, Sol. Energy Mater. Sol. Cells. 93 (2009) 2–5. doi:10.1016/j.solmat.2007.12.002.

[28] S.S. Latthe, S. An, S. Jin, S.S. Yoon, High energy electron beam irradiated TiO_2 photoanodes for improved water splitting, J. Mater. Chem. A. 1 (2013) 13567–13575. doi:10.1039/c3ta13481d.

[29] P.P. Shanbogh, V.C. Petwal, J. Dwivedi, A. Rao, N.G. Sundaram, High-Energy Electron-Beam-Induced Evolution of Secondary Phase and Enhanced Photocatalytic Activity in Monoclinic $BiEuWO_6$ Nanoparticles, J. Phys. Chem. C. 123 (2019) 10881–10892. doi:10.1021/acs.jpcc.8b12368.

[30] O. Dyck, S. Kim, S. V. Kalinin, S. Jesse, Placing single atoms in graphene with a scanning transmission electron microscope, Appl. Phys. Lett. 111 (2017). doi:10.1063/1.4998599.

[31] T. Furnival, R.K. Leary, E.C. Tyo, S. Vajda, Q.M. Ramasse, J.M. Thomas, P.D. Bristowe, P.A. Midgley, Anomalous diffusion of single metal atoms on a graphene oxide support, Chem. Phys. Lett. 683 (2017) 370–374.

doi:10.1016/j.cplett.2017.04.071.
[32] P. Lu, P. Yan, E. Romero, E.D. Spoerke, J.G. Zhang, C.M. Wang, Observation of electron-beam-induced phase evolution mimicking the effect of the charge-discharge cycle in Li-rich layered cathode materials used for Li ion batteries, Chem. Mater. 27 (2015) 1375–1380. doi:10.1021/cm5045573.
[33] A. V. Krasheninnikov, K. Nordlund, Ion and electron irradiation-induced effects in nanostructured materials, J. Appl. Phys. 107 (2010) 071301. doi:10.1063/1.3318261.
[34] M. Assis, M. Carvalho de Oliveira, T.R. Machado, N.G. Macedo, J.P.C. Costa, L. Gracia, J. Andrés, E. Longo, *In Situ* Growth of Bi Nanoparticles on $NaBiO_3$, δ-, and β-Bi_2O_3 Surfaces: Electron Irradiation and Theoretical Insights, J. Phys. Chem. C. 123 (2019) 5023–5030. doi:10.1021/acs.jpcc.8b11566.
[35] L. Yao, S. Majumdar, L. Äkäslompolo, S. Inkinen, Q.H. Qin, S. Van Dijken, Electron-beam-induced perovskite-brownmillerite-perovskite structural phase transitions in epitaxial $La_{2/3}Sr_{1/3}MnO_3$ films, Adv. Mater. 26 (2014) 2789–2793. doi:10.1002/adma.201305656.
[36] B. Christopher, A. Rao, B.S. Nagaraja, K. Shyam Prasad, G.S. Okram, G. Sanjeev, V.C. Petwal, V.P. Verma, J. Dwivedi, P. Poornesh, Correlation between structural and transport properties of electron beam irradiated $PrMnO_3$ compounds, Solid State Commun. 270 (2018) 30–37. doi:10.1016/j.ssc.2017.11.007.
[37] J. Li, Y. Li, Q. Li, Z. Wang, F. Leonard Deepak, Atomic-scale dynamic observation reveals temperature-dependent multistep nucleation pathways in crystallization, Nanoscale Horizons. 4 (2019) 1302–1309. doi:10.1039/c9nh00308h.
[38] J. Li, Z. Wang, F.L. Deepak, In Situ Atomic-Scale Observation of Droplet Coalescence Driven Nucleation and Growth at Liquid/Solid Interfaces, ACS Nano. 11 (2017) 5590–5597. doi:10.1021/acsnano.7b00943.
[39] J. Li, J. Chen, H. Wang, N. Chen, Z. Wang, L. Guo, F.L. Deepak, *In Situ* Atomic-Scale Study of Particle-Mediated Nucleation and Growth in Amorphous Bismuth to Nanocrystal Phase Transformation, Adv. Sci. 5 (2018) 1700992. doi:10.1002/advs.201700992.
[40] B.W. Smith, D.E. Luzzi, Electron irradiation effects in single wall carbon nanotubes, J. Appl. Phys. 90 (2001) 3509–3515. doi:10.1063/1.1383020.
[41] M. Terrones, Visualizing fullerene chemistry, Nat. Chem. 2 (2010) 82–83. doi:10.1038/nchem.526.
[42] I.G. Gonzalez-Martinez, A. Bachmatiuk, T. Gemming, B. Trzebicka, Z. Liu, M.H. Rummeli, Rapid synthesis of pristine graphene inside a transmission electron microscope using gold as catalyst, Commun. Chem. 2 (2019) 33. doi:10.1038/s42004-019-0134-3.
[43] A. Chuvilin, U. Kaiser, E. Bichoutskaia, N.A. Besley, A.N. Khlobystov, Direct transformation of graphene to fullerene, Nat. Chem. 2 (2010) 450–453. doi:10.1038/nchem.644.
[44] B.E. Mironov, H.M. Freeman, A.P. Brown, F.S. Hage, A.J. Scott, A.V.K.

Westwood, J.P. Da Costa, P. Weisbecker, R.M.D. Brydson, Electron irradiation of nuclear graphite studied by transmission electron microscopy and electron energy loss spectroscopy, Carbon. 83 (2015) 106–117. doi:10.1016/j.carbon.2014.11.019.

[45] I. Khan, J. Lan, P. Li, B. He, M. Gao, S. Huang, Electron-beam-induced uniform elongation of multi-walled carbon nanotube, SN Appl. Sci. 1 (2019) 1–8. doi:10.1007/s42452-019-1013-3.

[46] B. Buades, D. Moonshiram, T.P.H. Sidiropoulos, I. León, P. Schmidt, I. Pi, N. Di Palo, S.L. Cousin, A. Picón, F. Koppens, K. Biegert, Dispersive soft x-ray absorption fine-structure spectroscopy in graphite with an attosecond pulse, Optica. 5 (2018) 502–506.

[47] D. Golberg, Y. Bando, K. Kurashima, T. Sasaki, Fullerine and onion formation under electron irradiation of boron-doped graphite, Carbon. 37 (1999) 293–299.

[48] D. Ugarte, Formation mechanism of quasi-spherical carbon particles induced by electron bombardment, Chem. Phys. Lett. 207 (1993) 473–479.

[49] R. Pfeiffer, M. Holzweber, H. Peterlik, H. Kuzmany, Z. Liu, K. Suenaga, H. Kataura, Dynamics of carbon nanotube growth from fullerenes, Nano Lett. 7 (2007) 2428–2434. doi:10.1021/nl071107o.

[50] E. Hernández, V. Meunier, B.W. Smith, R. Rurali, H. Terrones, M. Buongiorno Nardelli, M. Terrones, D.E. Luzzi, J.C. Charlier, Fullerene coalescence in nanopeapods: A path to novel tubular carbon, Nano Lett. 3 (2003) 1037–1042. doi:10.1021/nl034283f.

[51] X. Li, W. Yang, B. Liu, Fullerene coalescence into metallic heterostructures in boron nitride nanotubes: A molecular dynamics study, Nano Lett. 7 (2007) 3709–3715. doi:10.1021/nl0720410.

[52] Y. Zhao, Y. Lin, B.I. Yakobson, Fullerene shape transformations via Stone-Wales bond rotations, Phys. Rev. B. 68 (2003) 233403. doi:10.1103/PhysRevB.68.233403.

[53] A.L. Balch, M.M. Olmstead, Reactions of transition metal complexes with fullerenes (C60, C70, etc.) and related materials, Chem. Rev. 98 (1998) 2123–2166. doi:10.1021/cr960040e.

[54] A.-C. Dupuis, The catalyst in the CCVD of carbon nanotubes - a review, Prog. Mater. Sci. 50 (2005) 929–961. doi:10.1016/j.pmatsci.2005.04.003.

[55] M.A. Pasha, A. Shafiekhani, M.A. Vesaghi, Hot filament CVD of Fe-Cr catalyst for thermal CVD carbon nanotube growth from liquid petroleum gas, Appl. Surf. Sci. 256 (2009) 1365–1371. doi:10.1016/j.apsusc.2009.08.090.

[56] K. Hernadi, A. Fonseca, J.B. Nagy, D. Bernaerts, A.A. Lucas, Fe-catalyzed carbon nanotube formation, Carbon. 34 (1996) 1249–1257. doi:10.1016/0008-6223(96)00074-7.

[57] C.M. Hsu, C.H. Lin, H.L. Chang, C.T. Kuo, Growth of the large area horizontally-aligned carbon nanotubes by ECR-CVD, Thin Solid Films. 420–421 (2002) 225–229. doi:10.1016/S0040-6090(02)00799-X.

[58] C. Klinke, J.M. Bonard, K. Kern, Comparative study of the catalytic growth of patterned carbon nanotube films, Surf. Sci. 492 (2001) 195–201. doi:10.1016/S0039-6028(01)01435-2.

[59] E.F. Kukovitsky, S.G. L'vov, N.A. Sainov, V.A. Shustov, L.A. Chernozatonskii, Correlation between metal catalyst particle size and carbon nanotube growth, Chem. Phys. Lett. 355 (2002) 497–503.

[60] Y. Shibuta, S. Maruyama, Molecular dynamics simulation of formation process of single-walled carbon nanotubes by CCVD method, Chem. P. 382 (2003) 381–386. doi:10.1016/j.cplett.2003.10.080.

[61] H. Dai, A.G. Rinzler, P. Nikolaev, A. Thess, D.T. Colbert, R.E. Smalley, Single-wall nanotubes produced by metal-catalyzed disproportionation of carbon monoxide, Chem. Phys. Lett. 4 (1996) 471–475.

[62] P. Nikolaev, M.J. Bronikowski, R.K. Bradley, F. Rohmund, D.T. Colbert, K.A. Smith, R.E. Smalley, Gas-phase catalytic growth of single-walled carbon nanotubes from carbon monoxide, Chem. Phys. Lett. 313 (1999) 91–97.

[63] G.G. Tibbetts, Why are carbon filaments tubular?, J. Cryst. Growth. 66 (1984) 632–638.

[64] V. León, M. Quintana, M.A. Herrero, J.L.G. Fierro, A. de la Hoz, M. Prato, E. Vázquez, Few-layer graphenes from ball-milling of graphite with melamine, Chem. Commun. 47 (2011) 10936–10938. doi:10.1039/c1cc14595a.

[65] N. Díez, A. Sliwak, S. Gryglewicz, B. Grzyb, G. Gryglewicz, Enhanced reduction of graphene oxide by high- pressure hydrothermal treatment, RSC Adv. 5 (2015) 81831–81837. doi:10.1039/C5RA14461B.

[66] S. Park, R.S. Ruoff, Chemical methods for the production of graphenes, Nat. Nanotechnol. 4 (2009) 45–47. doi:10.1038/nnano.2009.58.

[67] R. Raccichini, A. Varzi, S. Passerini, B. Scrosati, The role of graphene for electrochemical energy storage, Nat. Mater. 14 (2015) 271–279. doi:10.1038/NMAT4170.

[68] V. Georgakilas, M. Otyepka, A.B. Bourlinos, V. Chandra, N. Kim, K.C. Kemp, P. Hobza, R. Zboril, K.S. Kim, Functionalization of Graphene: Covalent and Non-Covalent Approaches, Derivatives and Applications, Chem. Rev. 112 (2012) 6156–6214. doi:10.1021/cr3000412.

[69] D. Ugarte, Curling and closure of graphitic networks under electron-beam irradiation, Nature. 359 (1992) 707–709.

[70] S. Hofmann, R. Sharma, C. Ducati, G. Du, C. Mattevi, C. Cepek, M. Cantoro, S. Pisana, A. Parvez, F. Cervantes-sodi, A.C. Ferrari, R. Dunin-borkowski, S. Lizzit, X.L. Petaccia, X.A. Goldoni, J. Robertson, *In situ* Observations of Catalyst Dynamics during Surface-Bound Carbon Nanotube Nucleation, Nano Lett. 7 (2007) 602–608. doi:10.1021/nl0624824.

[71] Z. He, J.L. Maurice, A. Gohier, C.S. Lee, D. Pribat, C.S. Cojocaru, Iron catalysts for the growth of carbon nanofibers: Fe, Fe_3C or both?, Chem. Mater. 23 (2011) 5379–5387. doi:10.1021/cm202315j.

[72] B.S. Xu, S.I. Tanaka, Formation of giant onion-like fullerenes under Al nanoparticles by electron irradiation, Acta Mater. 46 (1998) 5249–5257.

doi:10.1016/S1359-6454(98)00221-3.
[73] A.K. Geim, K.S. Novoselov, The rise of graphene, Nat. Mater. 6 (2007) 183–191.
[74] M.T. Lusk, L.D. Carr, Nanoengineering Defect Structures on Graphene, Phys. Rev. Lett. 100 (2008) 175503. doi:10.1103/PhysRevLett.100.175503.
[75] M.T. Lusk, D.T. Wu, L.D. Carr, Graphene nanoengineering and the inverse Stone-Thrower-Wales defect, Phys. Rev. B. 81 (2010) 155444. doi:10.1103/PhysRevB.81.155444.
[76] A. V Savin, Y.S. Kivshar, Localized defect modes in graphene, Phys. Rev. B. 88 (2013) 125417. doi:10.1103/PhysRevB.88.125417.
[77] B.W. Smith, D.E. Luzzi, Electron irradiation effects in single wall carbon nanotubes, J. Appl. Phys. 90 (2001) 3509–3515. doi:10.1063/1.1383020.
[78] S.T. Skowron, I. V Lebedeva, M. Popov, E. Bichoutskaia, Approaches to modelling irradiation-induced processes in transmission electron microscopy, Nanoscale. 5 (2013) 6677–6692. doi:10.1039/c3nr02130k.
[79] S. Kida, M. Yamamoto, K. Tada, H. Kawata, Y. Hirai, M. Yasuda, Correlation between electron-irradiation defects and applied stress in graphene: A molecular dynamics study, J. Vac. Sci. Technol. A. 33 (2015) 05E127. doi:10.1116/1.4928414.
[80] A. Van De Walle, A complete representation of structure-property relationships in crystals, Nat. Mater. 7 (2008) 455–458. doi:10.1038/nmat2200.
[81] N. Dwivedi, R.J. Yeo, N. Satyanarayana, S. Kundu, S. Tripathy, C.S. Bhatia, Understanding the role of nitrogen in plasma-assisted surface modification of magnetic recording media with and without ultrathin carbon overcoats, Sci. Rep. 5 (2015) 7772. doi:10.1038/srep07772.
[82] P. Trucano, R. Chen, Structure of graphite by neutron diffraction, Nature. 258 (1975) 136–137. doi:10.1038/258136a0.
[83] J. Wu, M. Lin, X. Cong, H. Liu, P. Tan, Raman spectroscopy of graphene-based materials and its applications in related devices, Chem. Soc. Rev. 47 (2018) 1822–1873. doi:10.1039/c6cs00915h.
[84] L.M. Malard, M.A. Pimenta, G. Dresselhaus, M.S. Dresselhaus, Raman spectroscopy in graphene, Phys. Rep. 473 (2009) 51–87. doi:10.1016/j.physrep.2009.02.003.
[85] S. Roscher, R. Hoffmann, O. Ambacher, Determination of the graphene-graphite ratio of graphene powder by Raman 2D band symmetry analysis, Anal. Methods. 11 (2019) 1180–1191. doi:10.1039/c8ay02619j.
[86] A.C. Ferrari, Raman spectroscopy of graphene and graphite: Disorder, electron-phonon coupling, doping and nonadiabatic effects, Solid State Commun. 143 (2007) 47–57. doi:10.1016/j.ssc.2007.03.052.
[87] S. Wang, Y. Dong, C. He, Y. Gao, N. Jia, Z. Chen, W. Song, The role of sp^2/sp^3 hybrid carbon regulation in the nonlinear optical properties of graphene oxide materials, RSC Adv. 7 (2017) 53643–53652. doi:10.1039/c7ra10505c.
[88] D. Joseph, N. Tyagi, A. Ghimire, K.E. Geckeler, A direct route towards preparing pH-sensitive graphene nanosheets with anti-cancer activity, RSC Adv.

4 (2014) 4085–4093. doi:10.1039/c3ra45984e.
[89] D. Ye, S.Q. Wu, Y. Yu, L. Liu, X.P. Lu, Y. Wu, Patterned graphene functionalization via mask-free scanning of micro-plasma jet under ambient condition, Appl. Phys. Lett. 104 (2014) 103105. doi:10.1063/1.4866788.
[90] P.R. Kumar, Y.H. Jung, K.K. Bharathi, C.H. Lim, D.K. Kim, High capacity and low cost spinel Fe_3O_4 for the Na-ion battery negative electrode materials, Electrochim. Acta. 146 (2014) 503–510. doi:10.1016/j.electacta.2014.09.081.
[91] L. V. Gasparov, K.-Y. Choi, G. Güntherodt, H. Berger, L. Forro, Electronic Raman scattering in magnetite, J. Appl. Phys. 101 (2013) 09G108. doi:10.1063/1.2709762.
[92] A.M. Jubb, H.C. Allen, Vibrational Spectroscopic Characterization of Hematite , Maghemite , and Magnetite Thin Films Produced by Vapor Deposition, ACS Appl. Mater. Interfaces. 2 (2010) 2804–2812. doi:10.1021/am1004943.
[93] A.C. Ferrari, J. Robertson, Interpretation of Raman spectra of disordered and amorphous carbon, Phys. Rev. B. 61 (2000) 14095–14107. doi:10.1007/BF02543693.
[94] M.M. Lucchese, F. Stavale, E.H.M. Ferreira, C. Vilani, M.V.O. Moutinho, R.B. Capaz, C.A. Achete, A. Jorio, Quantifying ion-induced defects and Raman relaxation length in graphene, Carbon. 48 (2010) 1592–1597. doi:10.1016/j.carbon.2009.12.057.
[95] D. Teweldebrhan, A.A. Balandin, Modification of graphene properties due to electron-beam irradiation, Appl. Phys. Lett. 94 (2009). doi:10.1063/1.3062851.
[96] N.C. Tombs, H.P. Rooksby, Structure transition and antiferromagnetism in magnetite, Acta Crystallogr. 4 (1951) 474–475. doi:10.1107/S0365110X51001549.
[97] V.Z. Mordkovich, Y. Shiratori, H. Hiraoka, Y. Takeuchi, Synthesis of multishell fullerenes by laser vaporization of composite carbon targets, Phys. Solid State. 44 (2002) 603–606. doi:10.1134/1.1470536.
[98] Q.L. Zhang, S.C. O'Brien, J.R. Heath, Y. Liu, R.F. Curl, H.W. Kroto, R.E. Smalley, Reactivity of Large Carbon Clusters: Spheroidal Carbon Shells and Their Possible Relevance to the Formation and Morphology of Soot, J. Phys. Chem. 90 (1986) 525–528.
[99] R. Langlet, P. Lambin, A. Mayer, P.P. Kuzhir, S.A. Maksimenko, Dipole polarizability of onion-like carbons and electromagnetic properties of their composites, Nanotechnology. 19 (2008) 115706. doi:10.1088/0957-4484/19/11/115706.
[100] A. Camisasca, S. Giordani, Carbon nano-onions in biomedical applications: promising theranostic agents, Inorganica Chim. Acta. 468 (2017) 67–76. doi:10.1016/j.ica.2017.06.009.
[101] J.W. Martin, G.J. McIntosh, R. Arul, R.N. Oosterbeek, M. Kraft, T. Söhnel, Giant fullerene formation through thermal treatment of fullerene soot, Carbon. 125 (2017) 132–138. doi:10.1016/j.carbon.2017.09.045.
[102] H. Kroto, Space, Stars, C_{60}, and Soot, Science (80-.). 242 (1988) 1139–1145.
[103] H.W. Kroto, K.R. Heath, S.C. O'Brien, R.F. Curl, R.E. Smalley, C_{60}:

Buckminsterfullerene, Nature. 318 (1985) 162–163.
[104] J.P. Lu, W. Yang, Shape of large single- and multiple-shell fullerenes, Phys. Rev. B. 49 (1994) 11421–11424. doi:10.1103/PhysRevB.49.11421.
[105] D. Ugarte, Graphitic Nanoparticles, MRS Bull. 19 (1994) 39–42. doi:10.1557/S0883769400048399.
[106] S. Iijima, The 60-Carbon Cluster Has Been Revealed!, J. Phys. Chem. 91 (1987) 3467–3474. doi:10.1021/j100297a003.
[107] H. Terrones, M. Terrones, The transformation of polyhedral particles into graphitic onions, J. Phys. Chem. Solids. 58 (1997) 1789–1796.
[108] G. Cota-Sanchez, G. Soucy, A. Huczko, J. Beauvais, D. Drouin, Effect of iron catalyst on the synthesis of fullerenes and carbon nanotubes in induction plasma, J. Phys. Chem. B. 108 (2004) 19210–19217. doi:10.1021/jp047629z.
[109] C.T. Wirth, B.C. Bayer, A.D. Gamalski, S. Esconjauregui, R.S. Weatherup, C. Ducati, C. Baehtz, J. Robertson, S. Hofmann, The phase of iron catalyst nanoparticles during carbon nanotube growth, Chem. Mater. 24 (2012) 4633–4640. doi:10.1021/cm301402g.
[110] S. Renu, M. Edward, R. Peter, M.J.T. Michael, Site-Specific Fabrication of Fe Particles for Carbon Nanotube Growth, Nano Lett. 9 (2009) 689–694. doi:10.1021/nl803180e.
[111] L.C. Campos, V.R. Manfrinato, J.D. Sanchez-Yamagishi, J. Kong, P. Jarillo-Herrero, Anisotropic etching and nanoribbon formation in single-layer graphene, Nano Lett. 9 (2009) 2600–2604. doi:10.1021/nl900811r.
[112] J. Zhang, F.L. Bowles, D.W. Bearden, W.K. Ray, T. Fuhrer, Y. Ye, C. Dixon, K. Harich, R.F. Helm, M.M. Olmstead, A.L. Balch, H.C. Dorn, A missing link in the transformation from asymmetric to symmetric metallofullerene cages implies a top-down fullerene formation mechanism, Nat. Chem. (2013) 1–6. doi:10.1038/nchem.1748.
[113] M. Morel, E. Mosquera, D.E. Diaz-Droguett, N. Carvajal, M. Roble, V. Rojas, R. Espinoza-González, Mineral magnetite as precursor in the synthesis of multi-walled carbon nanotubes and their capabilities of hydrogen adsorption, Int. J. Hydrogen Energy. 40 (2015) 15540–15548. doi:10.1016/j.ijhydene.2015.09.112.

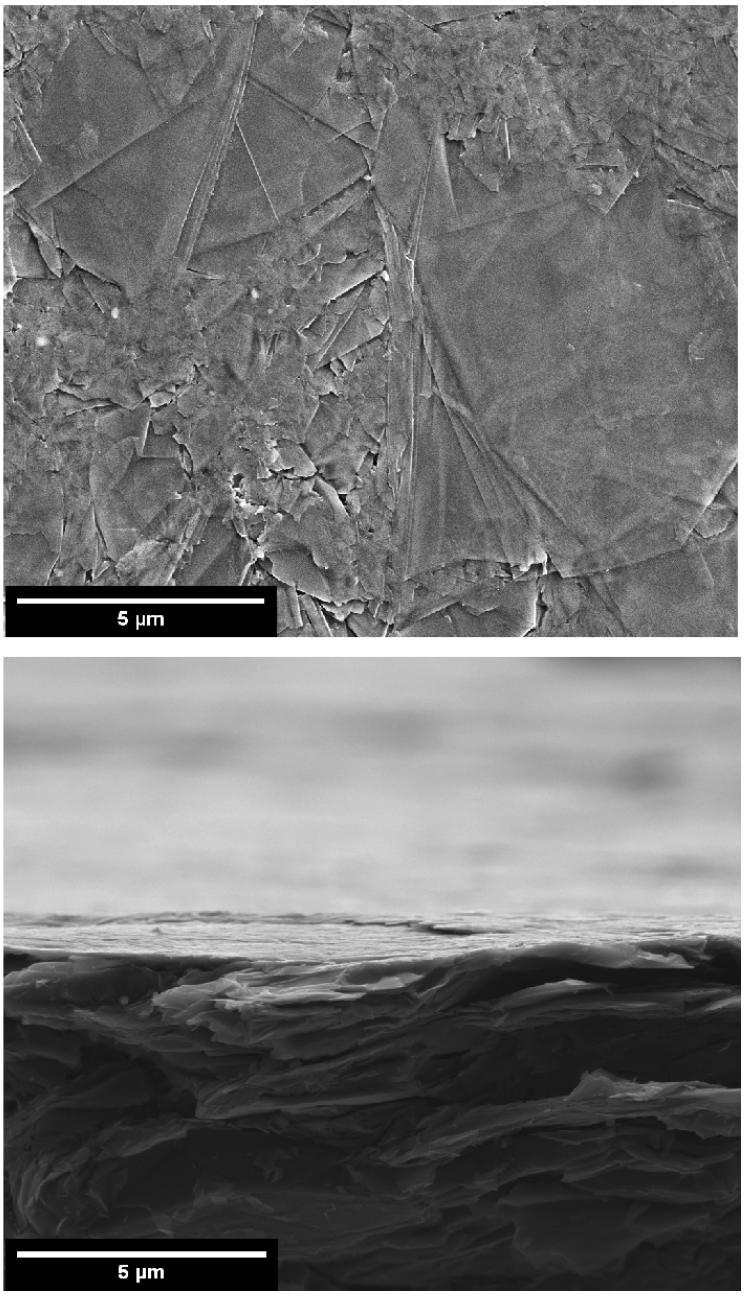

Fig S1 - FE-SEM images of the surface and cross-section of pristine carbon